RESEARCH ARTICLE

Identifying and Removing Interference and Artifacts in Multifractal Signals With Application to EEG Signals

BECHIR HBIBI [1,2,3], **CYRINE KHIARI**[1], **KARLTON WIRSING** [3], **(Senior Member, IEEE)**, **LAMINE MILI** [3], **(Life Fellow, IEEE)**, **KAMEL BACCAR**[2], **AND ABDELKADER MAMI**[1]

[1]Application Laboratory of Energy Efficiency and Renewable Energies, Faculty of Sciences of Tunis, University of Tunis El Manar, Tunis 1068, Tunisia
[2]Intensive Care and Anesthesia Department, National Institute of Neurology, Tunis 1007, Tunisia
[3]Department of Electrical and Computer Engineering, Virginia Polytechnic Institute and State University, Falls Church, VA 22043, USA

Corresponding author: Lamine Mili (lmili@vt.edu)

ABSTRACT Recorded Electroencephalogram (EEG) signals are typically affected by interference and artifacts, which can both impact eye reading and computer analysis of the data. Artifacts are induced by physiological (noncerebral) activities of the patient, such as muscular activities of the eyes, or the heart, or the body, while interference may be of external or internal origin. External interference can be induced by electrical machines if the latter are in the same room as the patients, while internal interference can be caused by abnormal breathing, or body movement, or electrode malfunction, or headset movements. Interference may cause severe distortion of EEG signals, resulting in loss of some segments of brain signals, while artifacts are additive signals to brain signals. Therefore, in order to analyze the brain activity signals of a patient, we need to identify and eliminate interference and isolate artifacts. In this paper, we analyze the EEG signals that were recorded using a headset with fourteen channels placed on the heads of comatose patients at the National Institute of Neurology in Tunis, Tunisia. We identify the interference using a robust statistical method known as projection statistics and we separate the brain signals from the artifacts cited above by applying an independent component analysis method. Finally, we show the multifractal behavior of the EEG signals without interference by applying the wavelet leader method and analyze their properties using the singularity spectrum.

INDEX TERMS Electroencephalogram signals, artifacts, interference, independent component analysis, projection statistics, multifractal analysis, EEGlab toolbox.

I. INTRODUCTION

EEG signals are recordings of the bioelectric activity of the brain using electrodes placed on the scalp of a person [1]. Their real-time analyses using the brain-computer interface have made remarkable progress in recent years [2]. These analyzes provide valuable information about the neural activities of the brain, allowing us to perform diagnostic tests of brain diseases such as epilepsy and metabolic encephalopathy, among others. However, EEG recordings suffer from two major problems that stem from their vulnerabilities to (1) interference picked up by the electrodes

The associate editor coordinating the review of this manuscript and approving it for publication was Gerardo Di Martino .

from the environment or the human body and (2) artifacts caused by the physiological activities of the body. In order to overcome these problems, many approaches and techniques have been proposed in the literature [3], which can be grouped as follows.

1) *Deletion*: Abnormal segments of an EEG signal that strongly deviate from the remaining part are manually identified and deleted [3]. However, this method is unreliable because it may either miss the detection of interference signal segments or delete valuable EEG signal segments.

2) *Filtering*: A number of signal filtering techniques have been proposed to improve EEG recorded

signals [4], [5]. The most efficient ones include a band-pass filter where the lower cut-off frequency is selected between 0.5Hz and 1Hz to reduce the electrode drift. For mobile EEG recordings, it is suggested to select a higher cut-off frequency in the range of 2Hz to 3Hz [6]. Concerning the upper cut-off frequency, it is chosen between 49Hz and 59Hz depending on the noise level in the region where the recordings are performed.

3) *Regression Methods*: Using regression methods, associated artifacts are removed by processing two different databases of EEG signals, which are recorded separately or simultaneously; here, one is marked as the reference database, while the other is marked as the headset database [7]. For example, in addition to the headset placed on the head of a patient, electrodes are also placed either on every eye to record the artifacts generated by eye blinking and eye movements, or on the heart, or on the neck muscles. Evidently, this approach will provide unreliable results if the artifacts occur simultaneously or if there is interference, which is typically the case in practice.

4) *Blind Source Separation* (*BSS*): This method is applied when only the mixed signals are available while both the source signals and the mixing functions are unknown. A version of BSS has been applied mainly to EEG signals as indicated in [8] and [9].

The most successful methods proposed by signal processing researchers and used by neurologists to isolate artifacts in recorded EEG signals without utilizing additional recorders are Independent Component Analysis (ICA) methods [10], [11]. These methods assume statistical independence and additive mixing of recorded signals. They have been applied to detect certain special brain activities such as epileptic activities [12] or to extract specific artifacts such as eye blinking [13] or skeletal muscle movements [14], to name a few. Despite their popularity, ICA methods do not provide good results when there is either (1) an insufficient number of electrodes that is smaller than that of the mixed signals, or (2) a high level of interference induced by the proximity of electrical machines, or (3) a distortion of the EEG signals due to the displacement of the headset from its initial position following the patient's head movement or the movement of a person near the headset when the latter is recording.

To overcome these weaknesses, in this paper, we propose to first estimate projection statistics to detect and remove the spikes of the EEG signals induced by interference. Projection statistic is a robust version of the classical Mahalanobis distance, which allows us to reliably identify and delete outliers in the EEG signals. Then, we execute an ICA method to separate the artifacts from the signals generated by the brain. Finally, we analyze the multifractal properties of segments of EEG signals without interference using the wavelet leader method and the derived singularity spectrum.

The paper is organized as follows. Section II defines and classifies the interference and artifacts of recorded EEG signals. Section III defines the projection statistics and provides the algorithm for their calculation. Section IV outlines the most popular ICA methods. Section V reveals the multifractal properties of the EEG signals using the wavelet leader and the bootstrapping method. Section VI highlights the properties of the recorded EEG signals. Section VII provides conclusions and outlines some future work.

II. INTERFERENCE AND ARTIFACTS OF THE RECORDED EEG SIGNALS

A. SIGNAL RECORDINGS

The recordings were made with an EMOTIV EPOC X-14 channel wireless EEG headset. The 14 headset channels are labeled AF3, F7, F3, FC5, T7, P7, O1, O2, P8, T8, FC6, F4, F8, and AF4. The headset was wirelessly connected to an Intel Core i3 laptop, which is placed between 1 and 2 meters from a patient. The sampling rate was set at 256 Hz with a filter band of 1Hz to 49Hz. More than 50 signals were recorded from 22 patients. Among them, we chose only 15 signals to be cleaned from interference and separated into artifacts components and brain signals components. These signals contain all the interference and artifacts that may affect a recorded EEG signal from a comatose patient in an intensive care room.

B. INTERFERENCE

Definition 1: An interference is a distortion of the EEG signal that results in the loss of some segments of the brain signal.

The causes of internal and external interference include the following:

- *Electrodermal activity*: Electrodermal interference originates from changes in the electrolyte concentration of the EEG electrodes.
- *Heavy breathing and respiratory devices*: Chest movements due to breathing can induce movements of the head and therefore of the electrodes on the pillow, resulting in slow and rhythmic potential changes in these electrodes. Heavy breathing from a comatose patient causes a distortion in the EEG signal.
- *Abnormal movements*: Small and a fortiori large movements of a comatose patient affect the EEG signals by causing deviations of the EEG electrodes. Furthermore, the movements of another person near the EEG headset disturb the EEG signal, especially if it is a portable headset.
- *Electric machines*: External interference is induced by the electric machines located in the reanimation room.

C. ARTIFACTS

Definition 2: An artifact is an additive signal to the brain signal that is not a noise.

Artifacts are classified as follows:

- *Ocular* (*EOG*): Ocular artifacts, known as EOG artifacts, are of two types. The first type is caused by the six extraocular muscles that move the eye, which are the superior rectus, inferior rectus, lateral rectus, medial rectus, superior oblique, and inferior oblique.

The second type is caused by the movements of the eyelids (blinks). Slow or rapid eye movements contaminate EEG signals because they induce changes in the electric fields around the eyes due to eye movement. Artifacts due to vertical or horizontal eye movements can have large amplitudes. The former are found at the front polar sites, with an exponential decay towards the occipital sites, while the latter are found at the front temporal sites, with opposite signs for the left hemisphere, the right hemisphere, and a linear slope between these two extremes [12].

- *Muscular* (*EMG*): Muscle artifacts, known as EMG artifacts, are signals generated by different muscles in the body such as those in the hands, legs, or neck. They appear as isolated spikes or smooth signals. Their amplitudes vary from small to large. Scalp and neck muscle movements result in the largest amplitude artifacts because they are the closest to the electrodes.

- *Cardiac* (*ECG*): Cardiac artifacts, known as ECG artifacts, are generated by the heart. An ECG artifact is dependent on the orientation of the electrical dipole of the heart and is seen simultaneously on several sensors. Pulse artifacts, on the other hand, usually affect only one sensor as they are due to pulsating scalp arteries lying directly under the electrode.

It should be noted that, unlike interference, artifacts do not distort the brain signal.

D. ARTIFACTS AND INTERFERENCE IN REAL RECORDED SIGNALS

During the period when we recorded the EEG signals at the National Institute of Neurology in Tunis, we noticed the occurrence of real-time interference that is not only due to nearby electric machines, but also to unexpected movement of the patient's atrium or heavy breathing. This type of inference cannot be avoided. Another type of interference that occurs during intensive care treatment, which can be avoided, is caused by nurses who are moving around to clean or touch the head of the patient having a headset. To avoid these problems, it is recommended to make the recordings outside of nursing periods. Regarding EOG artifacts, they occur only when the patient is awake. Therefore, they can be avoided by making recordings during the period when the patient is sleeping. Another action that can affect the recorded EEG signals and that can be avoided is someone touching the bottom of the electric machines.

As shown in Figs. 1 and 2, the signals registered in intensive care patients are the most contaminated. They are also the most challenging to analyze. Indeed, in Fig. 1, a high-amplitude interference affected Channel T8 for one-second duration starting from 56th second. This does not have an important impact on the visual reading and analysis of the signals, but surely affects the multifractal properties and leads to a poor analysis of the EEG signals.

Regarding the EEG signals shown in Fig. 2, we observe that they are significantly more contaminated than the ones
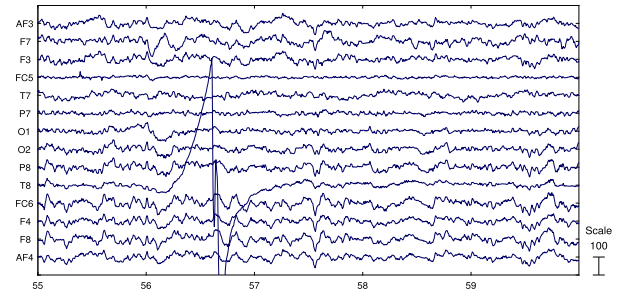

FIGURE 1. Significant interference affects one EEG signal recorded on Channel T8 from a comatose patient in the intensive care room.
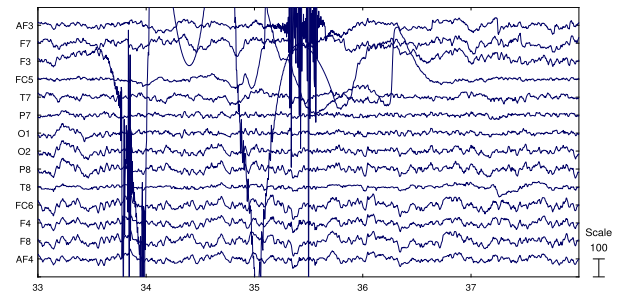

FIGURE 2. Significant interference affects the lower EEG signal recorded on Channel AF4 and the four upper signals recorded on Channels FC5, F3, F7, and AF3 from a comatose patient in the intensive care room.

shown in Fig. 1. Concretely, significant interference affects the lower signal around 34th second and the upper four signals from 35th second to 37th second, making visual reading impossible. Analyzing the multifractal aspect of this part of the data is also impossible. Most neuroscience analysts and doctors ignore this portion of the data and, as a result, they lose a large amount of clean data because of the contaminated channels AF3, F3, and FC5. We can also see some minor artifacts in Channels O1, O2, P8 around 33.2^{th} second. We call into question the traditional methods of using additional sensors to capture and remove environmental noises. By contrast, automated processing of contaminated signals allows us to analyze and model them without the need of human intervention. In this paper, we propose to first identify and remove interference using projection statistics and then apply the ICA method to separate artifacts from brain signals.

III. PROJECTION STATISTICS

Outliers may occur in EEG signals in many different ways. For instance, they may occur due to either interference from other medical instruments located in the room or large communication noises that have the same amplitudes as the brain signals of the patient. In that case, the identification of outliers becomes much more difficult and requires sophisticated algorithms to ensure reliability.

The conventional method to identify outliers in a multivariate point cloud is based on the Mahalanobis Distance (MD), which is a measure of the distance of the associated point with respect to the bulk of the point cloud. The MD of an n-dimensional vector, $\mathbf{h}_i$, which is the i-th column vector of

the observation matrix $\mathbf{H}^T$ and has a sample mean given by $\bar{\mathbf{h}}$ and a sample covariance matrix given by $\hat{\mathbf{C}}$, is defined as

$$MD_i = \sqrt{(\mathbf{h}_i - \bar{\mathbf{h}})^T \hat{\mathbf{C}}^{-1}(\mathbf{h}_i - \bar{\mathbf{h}})}. \tag{1}$$

If we assume that the $\mathbf{h}_i$'s are drawn from a normal distribution, $N(\mu, \mathbf{C})$, then MD_i^2 will approximately obey a chi-squared distribution with n-degrees of freedom, that is, χ_n^2. The classic outlier identification method flags all data points having $MD_i > \sqrt{\chi_{n,0.975}^2}$. However, this method is not robust because it is prone to the masking effect; indeed, a sufficiently large outlier can bias the sample mean and inflates the sample covariance matrix to the point where a second outlier closer to the bulk will stand below the confidence threshold $\sqrt{\chi_{n,0.975}^2}$. As a result, the tolerance ellipsoid covers in part or in total the set of outliers, including the failure of the MD to reveal some or all of them, which can cause a total breakdown.

Stahel [15] and Donoho [16] independently showed that the MD can be written as

$$MD_i = \max_{\|\mathbf{v}\|=1} \frac{|\mathbf{h}_i^T \mathbf{v} - \mu(\mathbf{h}_1^T \mathbf{v}, \overset{\wedge}{\ldots}, \mathbf{h}_m^T \mathbf{v})|}{\hat{\sigma}(\mathbf{h}_1^T \mathbf{v}, \ldots, \mathbf{h}_m^T \mathbf{v})}, \tag{2}$$

where $\hat{\mu}$ and $\hat{\sigma}$ are the sample mean and the sample standard deviation of the projections of the data points $\mathbf{h}_i$ on the direction of the vector $\mathbf{v}$. It is well-known that the sample mean and sample standard deviation estimates are not robust against outliers.

Motivated by (2), Stahel [15] and Donoho [16] proposed a robust version of the MD by replacing the sample mean with the sample median and the sample standard deviation with the Median-Absolute Deviation (MAD) from the median, which is defined as

$$MAD = 1.4826 \underset{i}{med} |\mathbf{h}_i^T \mathbf{v} - \underset{j}{med}(\mathbf{h}_j^T \mathbf{v})|. \tag{3}$$

Specifically, a PS of a multivariate data point relative to a multivariate point cloud is defined as the maximum of the absolute values of the standardized projections of that data point on the straight lines that pass through the coordinate-wise median and the data points [17]. We can then write the robust version of the projection statistic as

$$PS_i = \max_{\|\mathbf{v}\|=1} \frac{|\mathbf{h}_i^T \mathbf{v} - \underset{i}{median}(\mathbf{h}_1^T \mathbf{v}, \ldots, \mathbf{h}_m^T \mathbf{v})|}{1.4826\, c_m \underset{i}{median} |\mathbf{h}_i^T \mathbf{v} - \underset{j}{median}(\mathbf{h}_j^T \mathbf{v})|}. \tag{4}$$

Here, the maximum is taken over all the normalized vectors $\mathbf{v}$, that originate from the coordinate-wise median of the vectors, $\mathbf{h}_i$. As for the constant $\mathbf{c_m}$, it is a dimensionality correction factor, which is defined as

$$c_m = 1 + \frac{15}{m-n}, \tag{5}$$

where m is the number of datapoints and n is the number of dimensions. Typically, m is much larger than n. But because it is not practical to consider all possible directions as described

above, Gasko and Dohoho [18] proposed to investigate only those directions originating from the coordinate-wise median of the point cloud and passing through each of the data points, yielding a total of directions equal to m to be examined. Given the observation matrix $\mathbf{H}$, the PSs are calculated using the algorithm described in Table 1.

TABLE 1. Projection statistics steps.

Step 1:	Calculate $\bar{M} = \{ \underset{j=1,\ldots,m}{med}(h_{j1}), \ldots, \underset{j=1,\ldots,m}{med}(h_{jn}) \}$
Step 2:	Calculate the directions $\bar{u}_j = \bar{h}_j - \bar{M}$
Step 3:	Normalize $\bar{u}_j$ to get $\bar{v}_j = \frac{\bar{u}_j}{\|\bar{u}_j\|} = \frac{\bar{u}_j}{\sqrt{u_{j1}^2 + \ldots + u_{jn}^2}}; j = 1, \ldots, m$
Step 4:	Calculate the standardized projections of $\bar{h}_1, \ldots, \bar{h}_m$ on $\bar{v}_j$. These standardized projects are given by $z_{1j} = \bar{h}_1^T \bar{v}_j$; $z_{2j} = \bar{h}_2^T \bar{v}_j; \ldots; z_{mj} = \bar{h}_m^T \bar{v}_j$
Step 5:	Calculate the median of $\{z_{1j}, \ldots, z_{mj}\} = z_{med,j}$
Step 6:	Calculate $MAD_j = 1.4826\, c \underset{i}{med} |z_{ij} - z_{med,j}|$ where $c = 15/(m-n)$
Step 7:	Calculate the standardized projections $P_{ij} = \frac{|z_{ij} - z_{med,j}|}{MAD_j}$ for $i = i, \ldots, m$
Step 8:	Repeat steps 4, 5, 6, and 7 for all vectors $(v_1, \ldots, v_m)$ to get the standardized projections: $(P_i1, P_i2, \ldots, P_im)$ for $(i = 1, \ldots, m)$.
Step 9:	Calculate the projection statistics $PS_i = \max P_{i1}, P_{i2}, \ldots, P_{im}$ for $i = 1, \ldots m$

IV. INDEPENDENT COMPONENT ANALYSIS

ICA is the most popular method used to recover the brain signals from recorded EEG signals. It is based on the assumption that the mixture of the recorded signals, denoted by X, is related to the source signals contained in S via

$$X = A S, \tag{6}$$

where A is the mixing matrix. The goal of ICA is to recover the signal S through the unmixing matrix W, which is defined as

$$W = A^{-1}. \tag{7}$$

Using an estimator $\hat{W}$ of W, the recovery signal S' of S is derived as

$$S' = \hat{W} X. \tag{8}$$

A number of algorithms were proposed in the literature to estimate W. One of them minimizes the mutual information of m stochastic signals, $s_i'(t)$, $i = 1, ..m$, contained in S', yielding

$$I(s_i'(t) = \sum_{i=1}^{m} H(s_i'(t)) - H(S'(t)), \tag{9}$$

where $H(s_i'(t))$ is the differential entropy defined as

$$H(s_i'(t)) = -\int p_{s_i'(t)}(\eta) \log p_{s_i'(t)}(\eta) d\eta. \tag{10}$$

Referring to (8), we can rewrite (9) as

$$I(s'(t)) = \sum_{i=1}^{m} H(s'_i(t)) - H(X(t)) - \log|\det W|. \quad (11)$$

Another popular method minimizes the negentropy of a stochastic signal, x(t), which is defined as

$$J(x(t)) = H(x_{Gauss}(t)) - H(x(t)), \quad (12)$$

where $x(t)$ and $x_{Gauss(t)}$ are Gaussian stochastic signals with the same covariance matrix.

An alternative method is the maximum a posteriori estimator based on the assumption that $p(\hat{X}(t))$ is the estimated probability density function of the mixed signal X(t). Formally, we have

$$\hat{p}(x(t)) = \frac{p_s(A^{-1}X(t))}{|\det A|}. \quad (13)$$

Hence, we can define the likelihood function of the mixed signal as

$$\begin{aligned} L(A) &= E[\log_2 \hat{p}(X(t))] \\ &= \int p_x(X(t)) \log_2 p_s(A^{-1}X(t))dx \\ &\quad - \log_2|\det A|. \end{aligned} \quad (14)$$

Referring to (14), we can write the log-likelihood function as follows:

$$L(W) \approx \frac{1}{n} \sum_{i=1}^{m} \log_2 p_s(WX(t)) + \log_2|\det W|, \quad (15)$$

where m is the number of the source signals and n is the number of the mixed signals. There are a few other methods that are less widely used, such as the nonlinear principal component analysis and the kurtosis maximization method. Because the minimization of the mutual information method and the Infomax method perform a simultaneous estimation of all the components and do not requite prior knowledge of the recorded signals, they may be considered as the two best methods proposed so far. To estimate the W matrix, a number of algorithms may be utilized. Next, we present two of the commonly used ones, the gradient descent algorithm and the quasi-Newton algorithm.

A. GRADIENT DESCENT ALGORITHM

As explained in [19] and [20], the gradient descent algorithm searches for the minimum of a function first by computing the gradient at an initial guess, then by moving in the opposite direction of the gradient with a suitable step, and finally by repeating this process until convergence is reached. A few modifications have been made to this algorithm to reduce its complexity, yielding the so-called stochastic gradient descent algorithm, as described in [21] and [22].

B. QUASI-NEWTON ALGORITHM

The first application of the quasi-Newton algorithm to the ICA of EEG signals was made by Palmer et al. [23]. Later, by comparing different iterative methods, Delorme et al. [24] and [25] concluded that this algorithm is the most effective one for the ICA application, as it does not involve any step parameter, while showing a fast convergence rate compared to the gradient descent algorithm.

V. MULTIFRACTAL PROPERTIES OF THE EEG SIGNALS

EEG signals are highly irregular signals with many interesting properties. Multifractal analysis, along with other analysis techniques, can help us identify the unique features of the signal. These features can then be compared to dynamics or chaos theory, other instances that have a known multifractal signature.

A fractal is an object for which one of its characteristics is replicated on many scales, leading to self-similarity. This object consists of either multiple copies of the same feature or multiple statistical copies. Unlike most objects that we are familiar with, the dimension of a fractal is usually not an integer. Fractal and multifractal behavior has been observed in many naturally occurring signals and phenomena as Mandelbrot [26] noted the following: "Clouds are not spheres, mountains are not cones, coastlines are not circles, and bark is not smooth, nor does lightning travel in a straight line." When the dimension is a spectrum of values, the signal is said to have a multifractal property; this can be seen as fractals intertwined with fractals.

Due to the high irregularity of the fractal signals, they are analyzed using the wavelet transform instead of the conventional Fourier transform [27], [28]. First developed by Haar [29], the wavelet transform decomposes a signal into a sum of basis functions that are in the time and frequency domains. The second advantage is that the coefficients produced are more numerically stable than those of the Fourier power spectrum. This is due to the fact that the phase transitions are localized in fractal analysis, but are spread throughout the Fourier power spectrum. The third advantage is that they can be applied to signals where the characteristic time scale is a significant fraction of the signal.

Progress in the wavelet transform was slow until the 1980s. Then, it speeded up with the development of the continuous wavelet transform by Grossmann and Morlet [30], which was expanded on by Stephen Mallat and other researchers [31]. The continuous wavelet transform produces a lot of redundant data because the transformed values of two different scales that differ slightly are highly correlated. On the other hand, the discrete wavelet transform uses only discrete values for the scales, typically a power of 2, and is invertible, which allows applications in noise removal and compression. Daubechies [32], [33], [34], [35] expanded the Haar transform by creating a compact transform with minimal overlap of information, known as the Daubechies wavelet family.
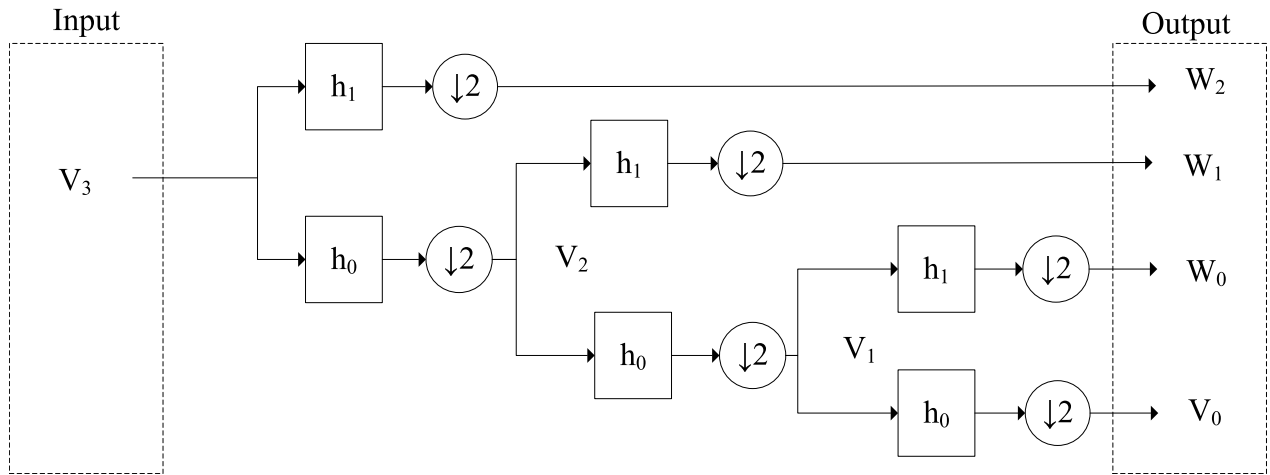
FIGURE 3. Diagram of a three level discrete wavelet transform [48].

Discrete wavelet transforms have been utilized in a number of applications in various forms along with neural networks and fuzzy logic. For example, they have been applied to detect faults in rotary equipment [36] and in induction motors [37]. They have been used in economics [38], in the JPEG 2000 compression standard [39], [40], and in medical image analysis such as mammogram image processing for the detection of breast cancer [41] and other ultrasound images [42]. Furthermore, they have been utilized to analyze EEG, ECG, and other human biometric signals [43], [44], [45], [46].

In [47], the Wavelet Transform Modulus Maxima (WTMM) and Multifractal Detrended Fluctuation Analysis (MFDFA) were used to calculate the singularity spectrum of EEG signals of healthy people and patients with paranoid schizophrenia and patients with depression. They showed that the width and position of the singularity spectrum differed between the groups. The width of the singularity spectrum indicates multifractality versus monofractality, while the position indicates persistence versus antipersistence. In this paper, we use the wavelet leader method with bootstrapping, which provides us with a more in-depth analysis of these signals.

A. DISCRETE WAVELET TRANSFORM
The discrete wavelet function is defined as

$$\psi_{j,k}(t) = \frac{1}{\sqrt{s_0^j}} \psi\left(\frac{t - \kappa \tau_0 s_0^j}{s_0^j}\right), \quad j, k \in \mathbb{Z}, \ s_0 > 1, \quad (16)$$

where j is the level of the wavelet transform; k is the position within that level; ψ is the base wavelet function; and $\psi_{j,k}$ is the wavelet function shifted in time and scale. An important property of the discrete wavelet transform is the concept of vanishing moments. The vanishing moment is the degree of the highest polynomial that can be suppressed by the wavelet.

A moment is defined as

$$\mu_n = \int x^k \psi(x) dx. \quad (17)$$

A vanishing moment makes the moment equal to zero, that is,

$$\int x^k \psi(x) dx = 0, \quad (18)$$

where k is its order. Each discrete wavelet function in its family is defined by the number of vanishing moments it has, with higher levels of the family having more vanishing moments. For example, the Haar wavelet function has one vanishing moment while Daubechies 2 has two vanishing moments. Since the discrete wavelet transform is often defined as a Finite Impulse Response (FIR) filter, the number of vanishing moments also corresponds to the number of coefficients in the filter. In the Daubechies wavelet family, for example, the number of coefficients in the filter is twice that of the number of vanishing moments. Vanishing moments eliminate polynomial trends in the data, which are expressed as

$$f(x) = g(x) + N(x). \quad (19)$$

With the discrete wavelet transform, each wavelet function, ψ, has a scaling function, ϕ. The relationship between ψ and ϕ is given by

$$\int \phi(x) \psi(x) dx = 1. \quad (20)$$

A diagram of the three level discrete wavelet transform is shown in Figure 3.

B. WAVELET LEADER METHOD
There are many different ways to detect multifractility in a signal. In this paper, we apply the wavelet leader method based on the discrete wavelet transform [49]. Wavelet leaders

utilize the Dyadic cube, which is known as the box covering in fractal analysis. It is defined as

$$\lambda = \left[\frac{k_1}{2^j}, \frac{k_1 + 1}{2^j}\right) \times \ldots \times \left[\frac{k_d}{2^j}, \frac{k_d + 1}{2^j}\right), \quad (21)$$

where $k = (k_1, \ldots, k_d) \in \mathbb{Z}^j$ and d is the topological dimension of the set. Wavelet leaders extend this procedure by making the dyadic cube given by (21) have the same center while being three times wider to cover the neighbors of the cube as well, which yields

$$\lambda = \left[\frac{k_1 - 1}{2^j}, \frac{k_1 + 2}{2^j}\right) \times \ldots \times \left[\frac{k_d - 1}{2^j}, \frac{k_d + 2}{2^j}\right], \quad (22)$$

$$h_\mu(x_0) = \lim_{j \to \infty} \inf \left(\frac{\log(\mu[3\lambda_j(x_0)])}{\log(2^{-j})}\right), \quad (23)$$

where μ is a non-negative measure of the set defined on $\mathbb{R}^d$. The discrete wavelet transform generates many coefficients that have small magnitudes, which can cause numerical instabilities with negative and fractional values. In addition to having one level of coarse coefficients, its output has, as shown in Figure 3, many levels of detail coefficients that are used by the wavelet leader method. The first level is calculated by taking the supremum of the absolute value of the detail coefficient and its two neighbors as follows:

$$L(1, k) = \sup \left\{|d_{1,k-1}|, |d_{1,k}|, |d_{1,k+1}|\right\}, \quad (24)$$

where k is the index of the detail coefficients. A well-known problem with the discrete wavelet transform is how to handle the edges. There are several solutions to deal with this problem; one of them is to exclude the edge coefficients, which is what the wavelet leader method does. Other solutions are mirroring or treating the coefficients beyond the edges as zero or some other constant, among others. The leaders for the subsequent levels are calculated from the supremum of the absolute value of the detail coefficient at that level along with the two neighboring leaders from the previous level as follows:

$$L(j, k) = \sup \left\{\begin{array}{l} L(j - 1, 2(k - 1) + 1), |d_(j, k)|, \\ L(j - 1, 2(k - 1) + 2) \end{array}\right\}, \quad (25)$$

where j is the level of the discrete wavelet transform.

Another way to enhance the numerical stability of the wavelet leader calculations is to apply a thresholding function when calculating the wavelet leader functions. Specifically, we set their values to zero when they are below a small threshold, ϵ, say 10^{-10}. The thresholded wavelet leader function is defined as

$$LQ_X(q, j, k) = \begin{cases} 0 & L_X(j, k) \leq \epsilon \\ L_X(j, k)^q & L_X(j, k) > \epsilon, \end{cases} \quad (26)$$

where q is the moment. A special case is $q = 0$, yielding a value of one for the thresholded wavelet leader function. The

structure function is defined as the average of the thresholded wavelet leader function over k, that is,

$$S^L(j, q) = \frac{1}{n_j} \sum_{k=1}^{n_j} LQ_X(q, j, k) = F_q |2^j|^{\zeta(q)}, \quad (27)$$

where n_j is the number of wavelet leaders at the level j of the discrete wavelet transform. The structure functions are calculated at several levels of q and j. A typical range for q ranges from -7 to 7 at fractional intervals, such as 0.1. Following [49], we derive the scaling function by rewriting (27) as

$$\mathbb{E} L_X(j, \cdot)^q = F_q 2^{j\zeta(q)}. \quad (28)$$

If (28) is finite, as is almost always the case, then we can rewrite it as follows.

$$\ln \mathbb{E} e^{q \ln L_X(j, \cdot)} = \sum_{p=1}^{\infty} C^L(j, q) \left(\frac{q^p}{p!}\right), \quad (29)$$

where $C^L(j, p)$ are the cumulants of order p of $\ln L_x(j)$ and p is an integer ≥ 1. Usually $p \leq 5$. This yields the singularity exponent function given by

$$\zeta(q) = \sum_{p=1}^{\infty} c_p \frac{q^p}{p!}. \quad (30)$$

From the scaling exponents, we take the Legendre transform, which yields the following dual equations:

$$D(h) = 1 + \min_q [qh - \zeta(q)], \quad (31)$$

and

$$\zeta(q) = 1 + \min_q [qh - D(h)]. \quad (32)$$

The Legendre transform is difficult to apply to actual data. Therefore, [49] proposed to use estimators based on the log-cumulant functions given by (29). The estimator of the scaling exponents $\zeta(q)$ is defined as

$$\hat{\zeta}(q) = \sum_{j=j_1}^{j_2} w_j \log_2 S^L(j, q), \quad (33)$$

and the estimator of the cumulant coefficients c_p is given by

$$\hat{c}_p = (\log_2 e) \sum_{j=j_1}^{j_2} w_j \hat{C}^L(j, p). \quad (34)$$

The estimators of $D(h)$ and h given by (31) and (32) expressed in terms of q are given by

$$\hat{D}(q) = \sum_{j=j_1}^{j_2} w_j U^L(j, q), \quad (35)$$

$$\hat{h}(q) = \sum_{j=j_1}^{j_2} w_j V^L(j, q). \quad (36)$$

Regarding $U^L(j, q)$, $V^L(j, q)$, $R_x^q(j, k)$, they are defined as follows:

$$U^L(j, q) = \sum_{k=1}^{n_j} R_x^q(j, k) \log_2 R_x^q(j, k) + \log_2 n_j, \quad (37)$$

$$V^L(j, q) = \sum_{k=1}^{n_j} R_x^q(j, k) \log_2 L_x(j, k), \quad (38)$$

$$R_x^q(j, k) = \frac{L_x(j, k)^q}{\sum_{k=1}^{n_j} L_x(j, k)^q}. \quad (39)$$

In (35) and (36), w are the weights assigned as the confidence given to each wavelet level. The set w must satisfy the following conditions:

$$\sum_{j=j_1}^{j_2} j w_j \equiv 1, \text{ and} \quad (40)$$

$$\sum_{j=j_1}^{j_2} w_j \equiv 0. \quad (41)$$

This yields the following solutions for w:

$$w_j = b_j \left(\frac{V_0 j - V_1}{V_0 V_2 - V_1^2} \right), \quad (42)$$

$$V_i = \sum_{j=j_1}^{j_2} j^i b_j, \ i = 0, 1, 2. \quad (43)$$

Here, b_j represents the confidence given to each cumulant or structure function. There are three possible settings for b_j. Setting b_j to 1 for all j yields an unweighted fit. The second possibility is to set b_j to $1/n_j$ for a weighted fit, where n_j is the number of wavelet leaders at level j. The third possibility is to set b_j as the reciprocal of the variance of bootstrapped estimates for level j, which is the one we are using for this paper.

C. BOOTSTRAPPING
When we are dealing with datasets, we usually only have one realization of a signal to analyze. Bootstrapping enables us to create multiple signals to analyze by resampling with replacement of the original signal [50]. This allows us to calculate confidence intervals for the signal, which Wendt et al. [51] proposed to do for the wavelet leader method. There is a short correlation with the discrete wavelet function, which must be taken into account when doing a bootstrapped resample of wavelet coefficients.

D. AUTOMATED RANGE SELECTION
The wavelet leader method requires you to select the j_1 and j_2 for the range in which to calculate the singularity spectrum. Some programs that have implemented the wavelet leader method do not require this, and they calculate the singularity spectrum over the entire range of discrete wavelet coefficients. However, the singularity spectrum may not exist over the entire range of the detail coefficients. For

implementations that offer range selection, usually the ranges that are selected are the ones that give the straightest line on a log/log scale. This can be error-prone and difficult to do for a large number of datasets. Automated range selection works by finding the range that minimizes the sum of squared residuals for the cumulants and the q functions [52]. The minimum number of levels is typically 3, but can be higher if desired. In addition, there can be different multifractals that exist over 2 adjacent ranges.

E. SURROGATE DATA TESTING
When dealing with nonlinear series, we generate surrogate data either by using the Fourier power spectrum or by shuffling the recorded data to test whether the hypothesis applies to the data, which is in this case the multifractal assumption [53]. To do this, multiple random copies of the data are created with the same property, and the test is applied to all of them. In the case of the Fourier power spectrum, we would create 2000 instances with the same Fourier power spectrum as the original signal, but the underlying data is different for each one.

F. ALTERNATIVE METHOD OF MULTIFRACTAL ANALYSIS
There are several other methods for multifractal analysis. One of them is MultiFractal Detrended Fluctuation Analysis (MFDFA) [54], [55], which is compared to the wavelet leader method. The Matlab code that implements this method is available in [56]. Currently, the bootstrap method and automated range analysis are not implemented for this method. This will need to be implemented in future work. MFDFA consists of the following main steps:

In Step 1, a profile of series is obtained by subtracting the mean from the signal and taking a cumulative sum as shown in the following equation:

$$Y(i) = \sum_{k=1}^{i} x_k - \langle x \rangle, \quad (44)$$

where i = 1, ... N, and where N is the total number of points.

In Step 2, the signal is decomposed into N_s segments of equal length, s. The total length of the signal does not have to be a multiple of s, which can leave a remainder at the end of the signal. When that occurs, the process is repeated starting at the end of the signal so that $2N_s$ are obtained. This is done so that the properties of the entire signal can be analyzed and the remainder is not ignored. This is shown in Fig. 4.

In Step 3, a polynomial fit is calculated for each segment using the least squares method, denoted as p_v, where v is the number of segments. This fit is subtracted from the series in step 1:

$$Y_s(i) = Y(i) - p_v(i). \quad (45)$$

Here, Y_s is the detrended segment for the segment size specified by s. The degree of the polynomial is one of the user-selected parameters for MFDFA.

In Step 4, the variance for each of the segments is calculated.

$$F_s^2(v) = \langle Y_s^2(i) \rangle = \frac{1}{s} \sum_{i=1}^{s} Y_s^2 [(v-1)s + i]. \quad (46)$$

In Step 5, the square root of the average of the variance calculated in Step 4 is taken to obtain the fluctuation function.

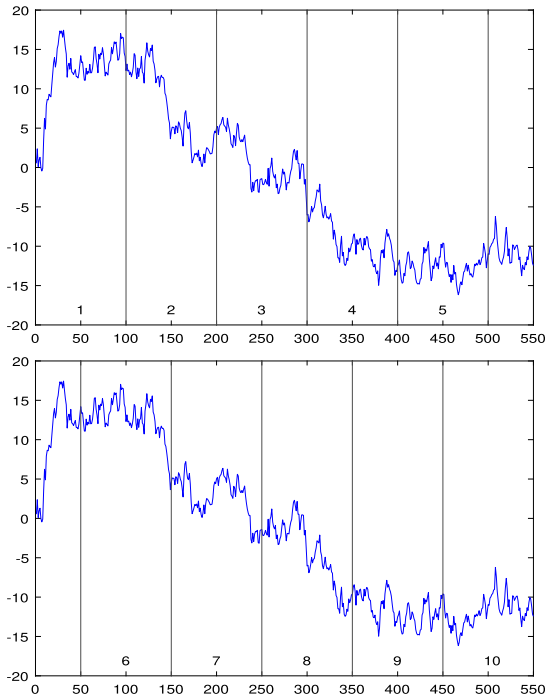$$F(s) = \left[\frac{1}{2N_s} \sum_{v=1}^{2N_s} F_s^2(v) \right]^{1/2}. \quad (47)$$

FIGURE 4. Brownian motion signal divided into equal segments of 100, showing how MFDFA handles signals that are not evenly divisible by the segment size.

For MFDFA, this equation is modified to calculate the fluctuations for each q as follows:

$$F(s) = \left[\frac{1}{2N_s} \sum_{v=1}^{2N_s} \left[F_s^2(v) \right]^{\frac{q}{2}} \right]^{1/q}. \quad (48)$$

When q = 2, this is the standard DFA calculation.

In Step 6, the scaling properties are estimated from the fluctuation functions previously calculated.

MFDFA shares some similarities with the wavelet leader method. For instance, the vanishing moments for the wavelet transform also remove polynomial trends from the data.

VI. ANALYSIS OF THE RECORDED EEG SIGNALS

The application of the wavelet method together with ICA improves the removal of artifacts from EEG signals, as mentioned in [57] and [58]. Furthermore, combining the Empirical Model Decomposition and the ICA (EMD-ICA) has a better performance for a specific application on EEG
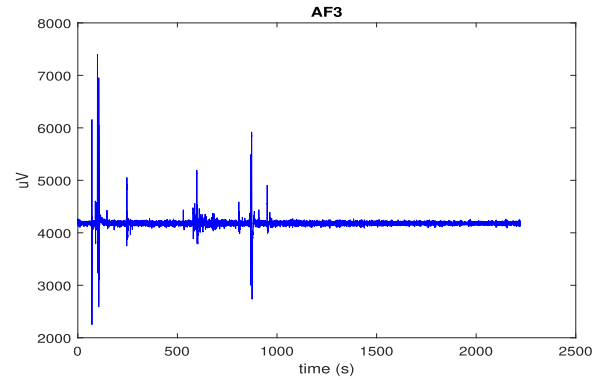
FIGURE 5. Short segment of an EEG signal recorded from a single channel EEG signal.
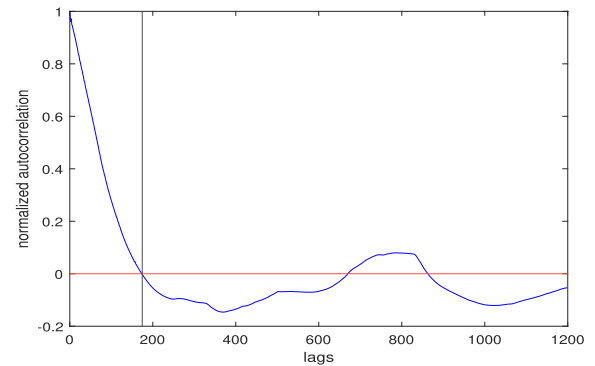
FIGURE 6. Normalized autocorrelation of the recorded EEG signal showing the first zero crossing between lag 174 and 175.

signals such as the removal of eye blinking [59], [60]. Last but not least, the analysis of the singularity spectrum and ICA of the EEG signals allows us to enhance the suppression of artifacts from a single channel as indicated in [60] and [61].

In this section, we analyze the recorded EEG signals by combining the two methods previously described, namely Projection Statistics and Independent Component Analysis (PS-ICA). First, we filter the data with a bandpass filter over the frequency range [1Hz, 49Hz] to avoid electrode and electricity line noise. Then, we apply the PS to remove the flagged outliers. Next, we replace the gaps that resulted from the removal of the outliers with a segment equal to the sample mean of the data in the channel. Finally, we apply AMICA, which is considered one of the best ICA algorithms [24].

A. IDENTIFICATION OF EXTERNAL INTERFERENCE USING PROJECTION STATISTICS

Fig. 8 displays a short segment of an EEG signal recorded from one headset channel. It clearly shows large amplitude spikes that are due to external interference. On the right-hand side of the signal plot, it is observed that there are no spikes as a result of interference. We use the autocorrelation function of the signal to determine the number of dimensions of the projection statistics. Based on mutual information, we look at where the autocorrelation function first crosses the horizontal axis, in this case between 173 and 174 as shown in Fig. 6. We use this value as the dimension of the signal. We apply

the PS to the signal to find the threshold that will be used to identify outliers. The signal on which we apply the PS has 284,800 data points. We implement a sliding window algorithm with a window size of 6000 and an increment of 100. This leads to that each data point has 60 different values of the PS, excluding the edges as shown in Fig. 9. We take the sample median of each of the 60 values, which yields a total of 284,400 values, which is equal to the number of data points as shown in Fig. 10. We sort the values from the sample median of the PS of the EEG signal and select a cut-off point, in this case, the 95% quantile as shown in Fig. 11 for the PS of the AF3 channel. We observe that the values increase sharply after that threshold. We apply the statistical test to the PS and identify the outliers. The outliers are shown in Fig. 12. These outliers are then deleted, and the different adjacent segments are joined as shown in Fig. 13. Note that the x-axis no longer refers to the time position of the signal because parts have been deleted. Due to the windowing, some outliers remain but have been sharply reduced.
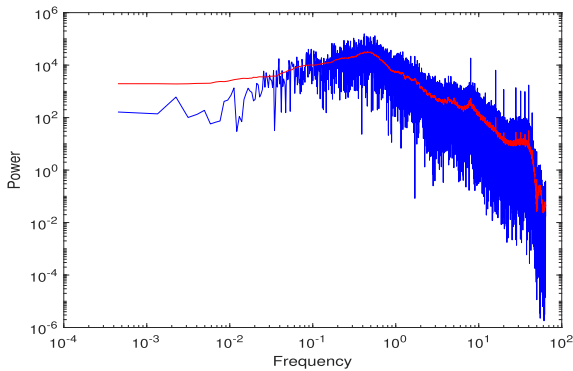
FIGURE 7. Fourier power spectrum of the clean section of the EEG signal on a log/log scale with the 101 position moving mean is shown in red. The power spectrum at zero frequency is excluded.
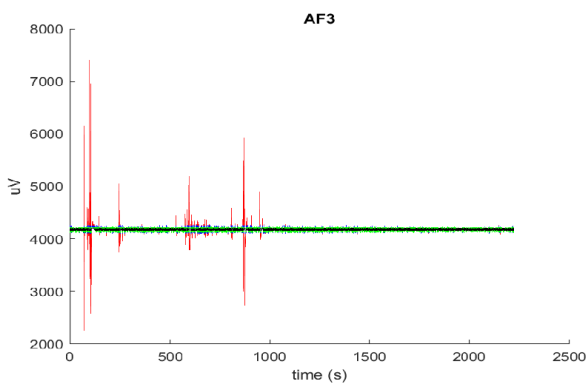
FIGURE 8. Recorded single-channel EEG signal shown in black, for which the signal segments highlighted in red are those that deviate more than 3 times the MAD.

B. REMOVAL OF INTERFERENCE AND ARTIFACTS

After the detection and removal of interference recognized as outliers by the PS algorithm, we fill the gaps by segments to make the ICA application useful. The results of the

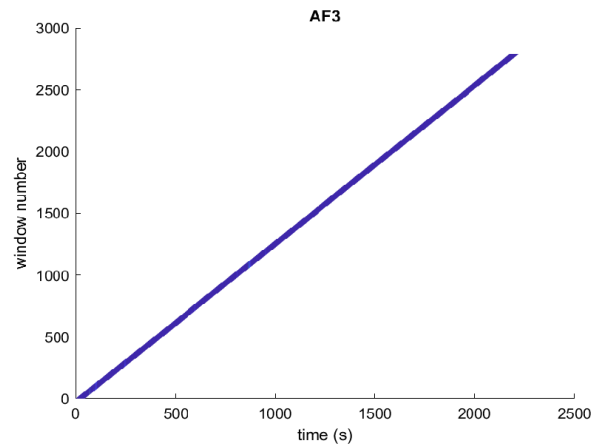application of our method presented in Section II-D are shown in Figs. 14 and 15.

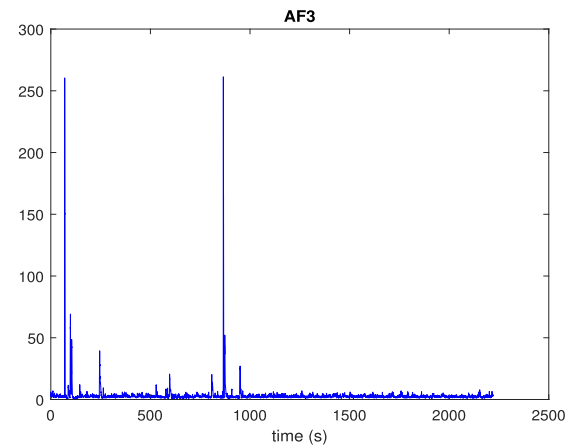**FIGURE 9.** Plot of the windowed projection statistics of the AF3 channel.

FIGURE 10. Plot of the windowed median projection statistics of the AF3 channel.
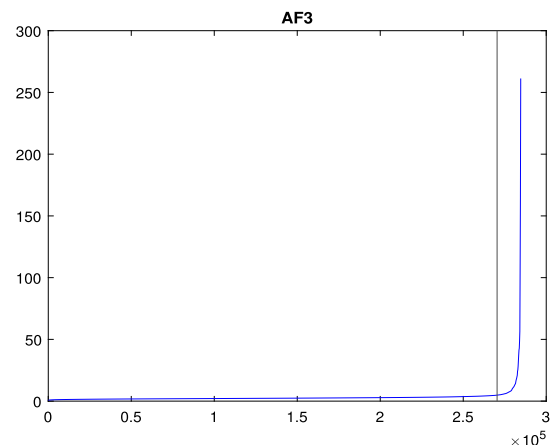

FIGURE 11. Plot of the sorted windowed median projection statistics of the AF3 channel with the 95% cutoff line displayed.

The results of applying PS to the data presented in Fig. 1, which is contaminated by one large interference in Channel T8, revealed the excellent ability of our method to remove all
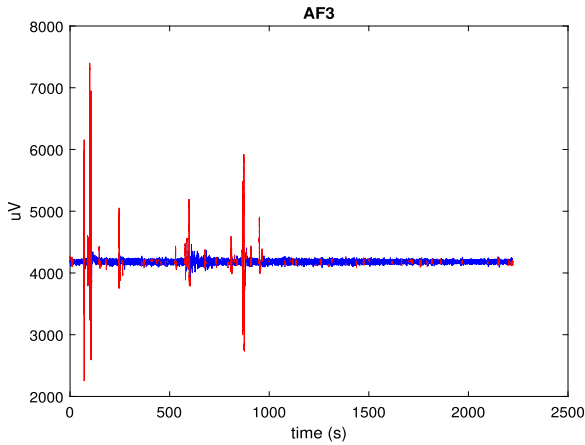
FIGURE 12. Plot of the AF3 channel with the outliers identified by windowed projection statistics in red.
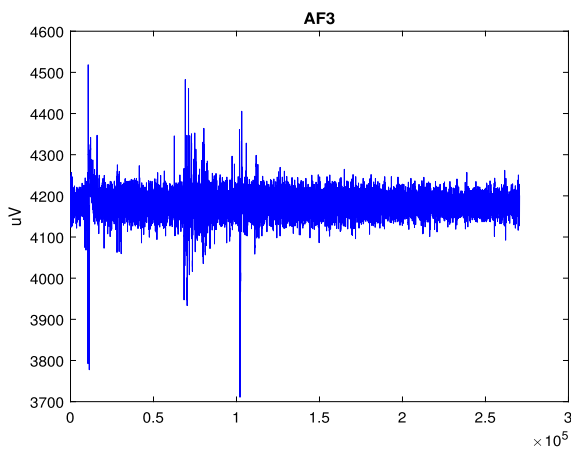

FIGURE 13. Plot of the AF3 channel with the outliers identified by windowed projection statistics removed.

contaminated data. The removed outliers are replaced by a straight line to make the application of the ICA possible for that part of the data (about 1 second) as shown in Fig. 14. As seen in Fig. 15, the PS method removes about 90% of the defective data in Fig. 2, but there are still some portions of interference in the signal. So far, reading the EEG signals by eyes has become possible, which allows us to avoid removing non-distorted signal segments of about 3 seconds of duration. To make this process automatic, we apply the PS for the second time and notice that 100 % of the interference has been removed. Then we apply the ICA approach using the AMICA algorithm of the EEGlab toolbox [62] to identify defective channels that contain artifacts. We realize that the ICA decomposition improves as the dataset is shorter. For this kind of problem, we prefer to use the ICA because of its ability to remove artifacts such as EOG, EMG, and others with small amplitudes that cannot be detected by the PS.

For the removal of flagged components after the application of the decomposition by the ICA, the removal of artifacts is possible by eyes or by some algorithms available on EEGLAB, such as the IC artifact classification MARA [63] or IClabel [64] for different kinds of artifacts. In the

case of the removal of a specific type of artifact, a number of algorithms are available. Here we site AAR [65] for the removal of EMG and EOG, the REGICA-Methodology [66] for automated EOG rejection, and the cleanline [67] for line noise rejection.

As indicated in [68], the AMICA algorithm can remove artifacts in a large number of channels. To verify this claim, we execute this algorithm on the recorded EEG signals for 5000 iterations; the higher the number of iterations, the better the performance of the AMICA algorithm will be. As shown to the left of Fig.16, an artifact severely affected all channels for about 0.3 s (marked green) and then another appeared with a smaller amplitude and a shorter period of time (marked in yellow). On the right of Fig.16, the results of the AMICA algorithm showed 13 artifact-free components and one affected one. The latter has to be removed or zeroed if needed for further application [69].

By removing both interference and artifacts presented in the intensive care room from the EEG channels with the conservation of the maximum possible clean data using two automatic methods, we make it possible to apply multifractal analysis or any other analysis without any human intervention. In the following, we analyze the multifractal properties of EEG signals recorded from comatose patients.
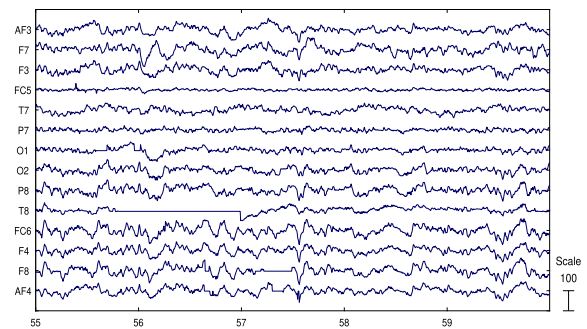

FIGURE 14. EEGLAB plot of the 14 EEG channels presented in Fig. 1 after the application of projection statistics.
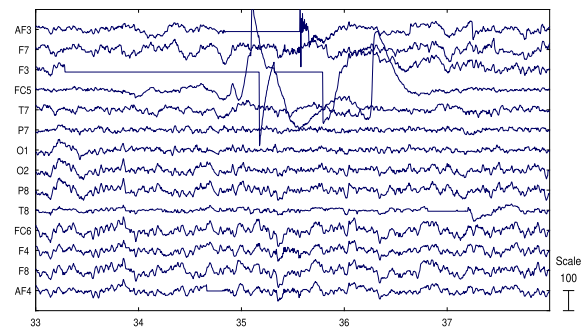

FIGURE 15. EEGLAB plot of the 14 EEG channels presented in Fig. 2 after the application of projection statistics.

C. DETERMINING THE MULTIFRACTAL PROPERTIES OF THE EEG SIGNAL

Applying the wavelet leader method with the bootstrapping technique, we find multifractal behavior occurring between
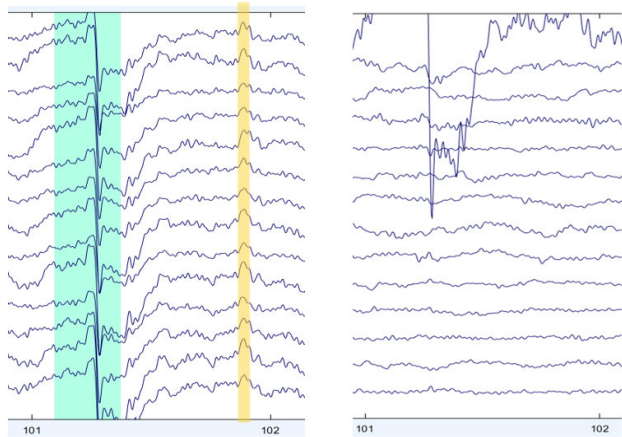
FIGURE 16. On the left EEG affected data in the hole 14 channels, on the right the 14 components after the application of the AMICA algorithm of the EEGLAB toolbox shows the reduction of artifact contamination to only one component.
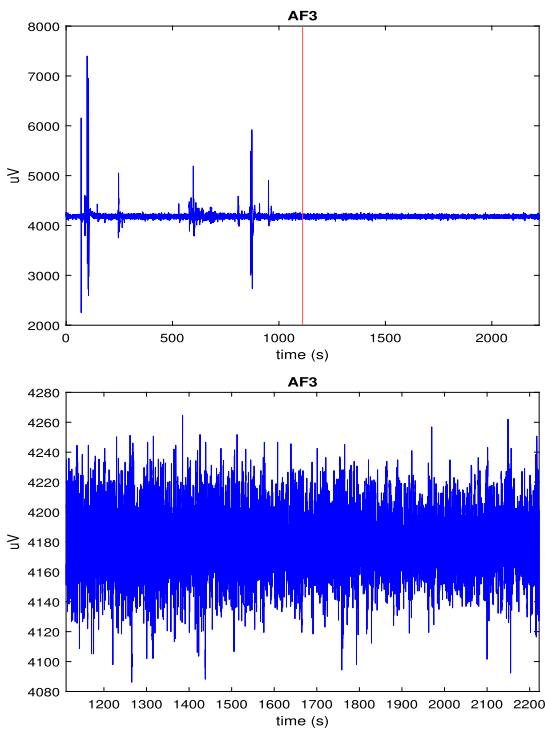

FIGURE 17. EEG signal that is used to analyze the multifractal spectrum. The part that is analyzed is to the right of the red line from time index 1111.13 seconds to the end.

Levels 9 and 11 of the clean, recorded EEG signal segment displayed in Fig. 17. This signal was sampled at a rate of 128 hertz. So these levels correspond to a sample rate between 0.25 Hz and 0.0625 Hz, that is, between 4 seconds and 16 seconds. Table 2 shows the relationship between the samples and the levels of the discrete wavelet transform for a signal sampled at 128 Hz. The scaling exponent and the singularity spectrum are shown in Fig. 18. The confidence intervals shown are the result of histograms obtained by bootstrapping. An example of histograms is displayed in Figs. 21 and 22. These are histograms representing the values
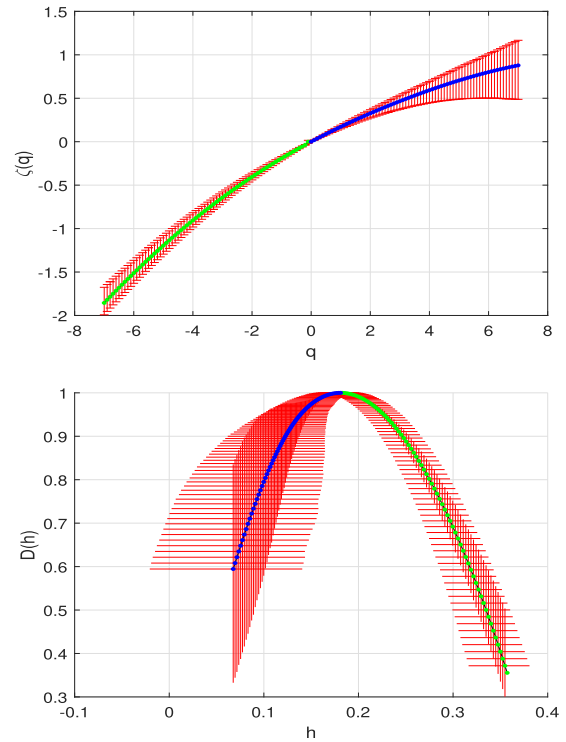

FIGURE 18. Scaling exponents and singularity spectrum at 25%-75% confidence intervals for levels 9-11 with 3 vanishing moments.
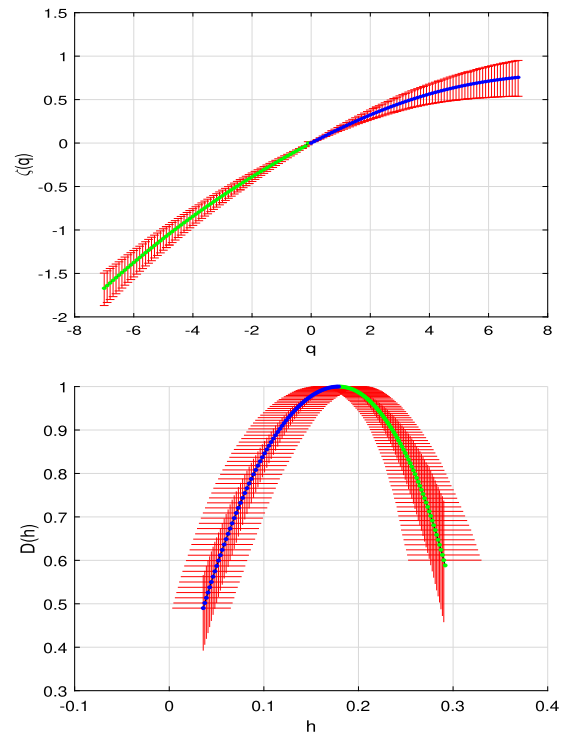

FIGURE 19. Scaling exponents and singularity spectrum at 25%-75% confidence intervals for levels 9-11 with 5 vanishing moments.

taken by the Hausdorff dimension, $D(h)$, versus the Holder exponent, h, for values of q equal to -7 and $+7$ shown in (31) and (32). The q values are the end points that have the largest confidence intervals. As shown in Fig. 23, the
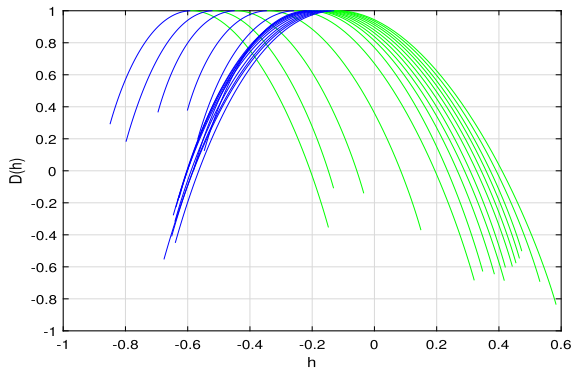
FIGURE 20. MFDFA calculation of the singularity spectrum for levels 9-11 with M set to 1-15.
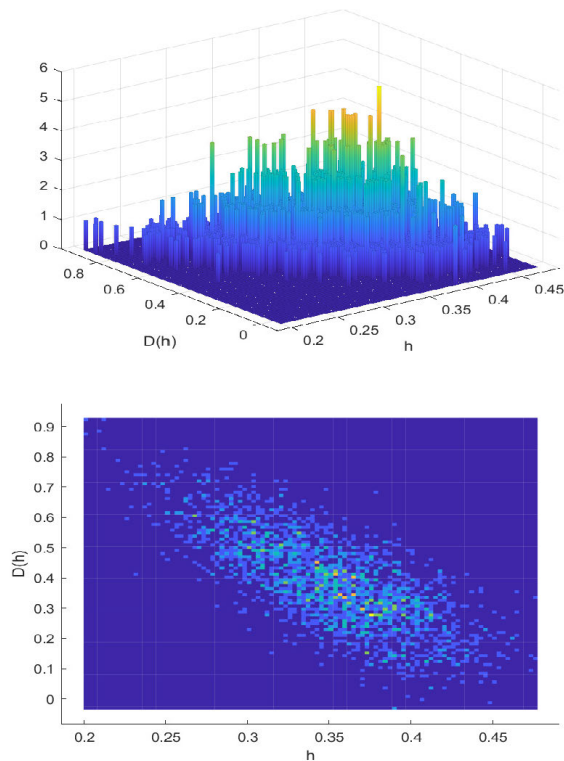
TABLE 2. Wavelet transform levels for a signal sampled at 128 hertz.

Level	Sample Rate (Hertz)	Time (Seconds)
0 (raw data)	128	0.007812
1	64	0.015625
2	32	0.031250
3	16	0.062500
4	8	0.125
5	4	0.25
6	2	0.5
7	1	1
8	0.5	2
9	0.25	4
10	0.125	8
11	0.062500	16
12	0.031250	32
13	0.015625	64
14	0.007812	128
15	0.003906	256
16	0.001953	512
17	0.000977	1024
18	0.000488	2048
19	0.000244	4096
20	0.000122	8192

FIGURE 21. 3D Histogram for q = −7 with 3 vanishing moments.
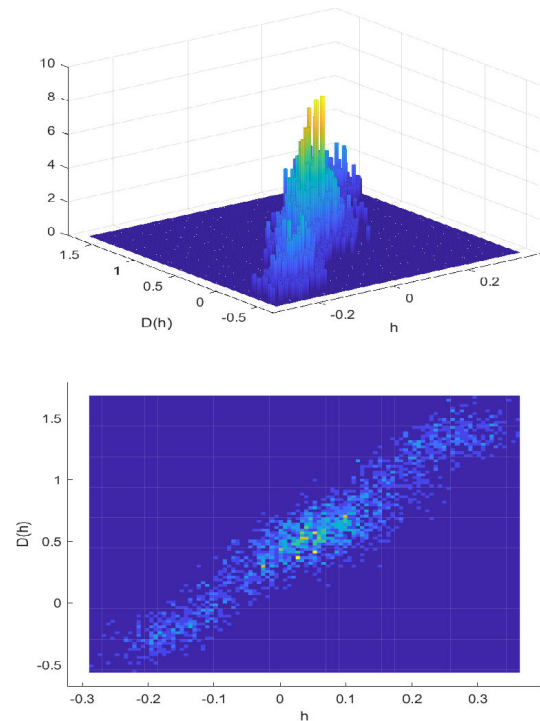

FIGURE 22. 3D Histogram for q = 7 with 3 vanishing moments.

TABLE 3. Cumulant values for 3 vanishing moments.

Cumulant	Value	STD	Reject	P-Value
c_1	0.181093	0.029892	1	0.00099950
c_2	−0.019776	0.009409	1	0.03698151
c_3	0.003164	0.003935	0	0.51374313
c_4	0.000072	0.001356	0	0.92353823
c_5	−0.000578	0.000738	0	0.27486257

shuffled surrogate data are represented by the light-shaded curve, the iterative amplitude adapted Fourier transform is represented by the dark-shaded curve, and the original signal is represented by the normal shaded curve. The surrogate signal for the IAAFT is approximately close to that of the original signal, which means that the multifractal properties of the signal are largely derived from the Fourier power spectrum of the signal, as shown in Fig. 7. On a log-log scale, we observe that it changes direction several times, indicating that it is not a fractal, but a multifractal signal. Changing the number of vanishing moments from 3 to 5 gives a slightly cleaner singularity spectrum and scaling exponents in Fig. 19. As observed in Table 3 and 4, the cumulative values are mostly the same for 3 vanishing moments and for 5 vanishing moments, respectively.

The results of the MFDFA analysis are shown in Fig. 20. Compared to the Wavelet Leader analysis, it showed more instability. The results showed a different spectrum for each of the M values chosen, with the results converging

TABLE 4. Cumulant values for 5 vanishing moments.

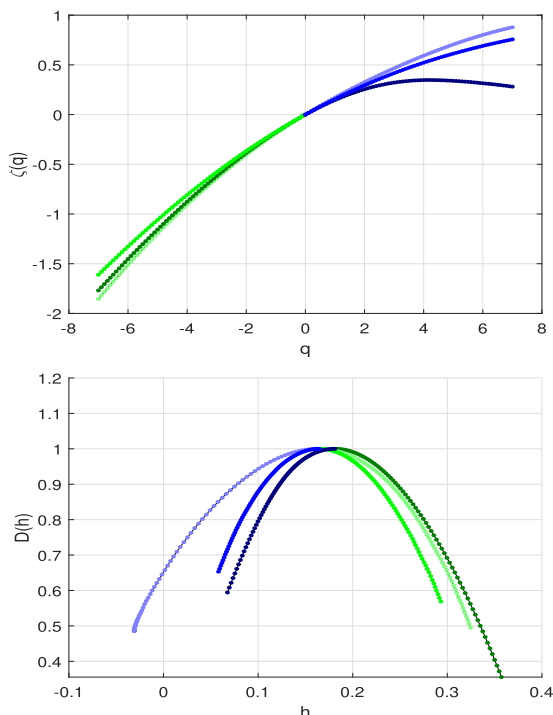| Cumulant	Value	STD	Reject	P-Value
c_1	0.178962	0.038629	1	0.00099950
c_2	−0.014163	0.008213	1	0.05397301
c_3	−0.001528	0.002557	0	0.52473763
c_4	−0.001674	0.001041	0	0.14692654
c_5	0.000241	0.000657	0	0.55472264

FIGURE 23. Surrogate scaling exponents and singularity spectrum with 3 vanishing moments. Blue curves represent positive q values and green curves represent negative q values. The shuffled surrogate data are represented by the light shaded curve, the iterative amplitude adapted Fourier transform is represented by the dark shaded curve, and the original signal is represented by the normal shaded curve.

around M = 6. Most MFDFA analysis consists of the use of polynomials with M from 1-3. In addition, the bootstrap technique has not been developed for MFDFA, so confidence intervals cannot be computed. Automated range analysis has also not been developed for the MFDFA method. Both techniques need to be developed in the future for MDFDA analysis. In this instance, the wavelet leader method gave better performance. The results were more stable across different wavelets.

VII. CONCLUSION AND FUTURE WORK
In this paper, we analyzed a set of EEG signals recorded from comatose patients in an intensive care room. First, we highlight the different causes of artifacts and interference that can affect EEG signals. We then applied PS to identify and remove interference from these signals. Next, we filled the gaps with straight lines equal to the sample medians of the remaining signals and applied an ICA method to separate the artifacts from the brain signals. Finally, we analyzed the multifractal properties of the EEG signals

using the wavelet leader and the singularity spectrum. In future work, we will investigate methods that will reduce the computing time of the PS. We will also study the dependence properties of the EEG signals using metrics based on copula estimation and we will apply machine learning methods to extract their features and classify them. The objective of this work is to characterize the different types of comatose states. Automated range analysis and bootstrapping need to be developed for other techniques of multifractal analysis as they have been developed for the wavelet leader method, so that multiple different multifractal analysis can be performed and compared.

REFERENCES
[1] D. E. Kusumandari, H. Fakhrurroja, A. Turnip, S. S. Hutagalung, B. Kumbara, and J. Simarmata, "Removal of EOG artifacts: Comparison of ICA algorithm from recording EEG," in *Proc. 2nd Int. Conf. Technol., Informat., Manage., Eng. Environ.*, Aug. 2014, pp. 335–339.

[2] W. Zgallai, J. T. Brown, A. Ibrahim, F. Mahmood, K. Mohammad, M. Khalfan, M. Mohammed, M. Salem, and N. Hamood, "Deep learning AI application to an EEG driven BCI smart wheelchair," in *Proc. Adv. Sci. Eng. Technol. Int. Conf. (ASET)*, Mar. 2019, pp. 1–5.

[3] M. K. Islam, A. Rastegarnia, and Z. Yang, "Methods for artifact detection and removal from scalp EEG: A review," *Clin. Neurophysiol.*, vol. 46, nos. 4–5, pp. 287–305, Nov. 2016.

[4] F. Lotte, "A tutorial on EEG signal-processing techniques for mental-state recognition in brain–computer interfaces," in *Guide to Brain–Computer Music Interfacing*, 2014, pp. 133–161.

[5] A. G. Correa, E. Laciar, H. D. Patiño, and M. E. Valentinuzzi, "Artifact removal from EEG signals using adaptive filters in cascade," *J. Phys., Conf. Ser.*, vol. 90, Nov. 2007, Art. no. 012081.

[6] M. Klug and K. Gramann, "Identifying key factors for improving ICA-based decomposition of EEG data in mobile and stationary experiments," *Eur. J. Neurosci.*, vol. 54, no. 12, pp. 8406–8420, 2021.

[7] G. L. Wallstrom, R. E. Kass, A. Miller, J. F. Cohn, and N. A. Fox, "Automatic correction of ocular artifacts in the EEG: A comparison of regression-based and component-based methods," *Int. J. Psychophysiol.*, vol. 53, no. 2, pp. 105–119, Jul. 2004.

[8] L. Shoker, S. Sanei, and J. Chambers, "Artifact removal from electroencephalograms using a hybrid BSS-SVM algorithm," *IEEE Signal Process. Lett.*, vol. 12, no. 10, pp. 721–724, Oct. 2005.

[9] T. Jung, S. Makeig, C. Humphries, T. Lee, M. J. McKeown, V. Iragui, and T. J. Sejnowski, "Removing electroencephalographic artifacts by blind source separation," *Psychophysiology*, vol. 37, no. 2, pp. 163–178, Mar. 2000.

[10] F. C. Viola, S. Debener, J. Thorne, and T. R. Schneider, "Using ICA for the analysis of multi-channel EEG data," in *Simultaneous EEG and fMRI: Recording, Analysis, and Application: Recording, Analysis, and Application*, 2010, pp. 121–133.

[11] L. Albera, A. Kachenoura, P. Comon, A. Karfoul, F. Wendling, L. Senhadji, and I. Merlet, "ICA-based EEG denoising: A comparative analysis of fifteen methods," *Bull. Polish Acad. Sci., Tech. Sci.*, vol. 60, no. 3, pp. 407–418, Dec. 2012.

[12] H. Nam, T. Yim, S. K. Han, J. Oh, and S. K. Lee, "Independent component analysis of ictal EEG in medial temporal lobe epilepsy," *Epilepsia*, vol. 43, no. 2, pp. 160–164, Feb. 2002.

[13] R. Li and J. C. Principe, "Blinking artifact removal in cognitive EEG data using ICA," in *Proc. Int. Conf. IEEE Eng. Med. Biol. Soc.*, Aug. 2006, pp. 5273–5276.

[14] B. W. Mcmenamin, A. J. Shackman, J. S. Maxwell, D. R. W. Bachhuber, A. M. Koppenhaver, L. L. Greischar, and R. J. Davidson, "Validation of ICA-based myogenic artifact correction for scalp and source-localized EEG," *NeuroImage*, vol. 49, no. 3, pp. 2416–2432, Feb. 2010.

[15] W. A. Stahel, "Robuste schätzungen. Infinitesimale optimalität und schätzungen von kovarianzmatrizen," Ph.D. dissertation, ETH Zurich, Zürich, Switzerland, 1981.

[16] D. L. Donoho, "Breakdown properties of multivariate location estimators," Harvard Univ., Boston, MA, USA, Tech. Rep., 1982.

[17] P. J. Rousseeuw and A. M. Leroy, *Robust Regression and Outlier Detection*. Hoboken, NJ, USA: Wiley, 1987.

[18] M. Gasko and D. L. Dohoho, "Influential observation in data analysis," in *American Statistical Association Proceedings of the Business and Economic Statistics Section*, 1982, pp. 104–109.

[19] S. Ruder, "An overview of gradient descent optimization algorithms," 2016, *arXiv:1609.04747*.

[20] S. E. Selvan, U. Amato, K. A. Gallivan, C. Qi, M. F. Carfora, M. Larobina, and B. Alfano, "Descent algorithms on oblique manifold for source-adaptive ICA contrast," *IEEE Trans. Neural Netw. Learn. Syst.*, vol. 23, no. 12, pp. 1930–1947, Dec. 2012.

[21] A. Sharma, "Guided stochastic gradient descent algorithm for inconsistent datasets," *Appl. Soft Comput.*, vol. 73, pp. 1068–1080, Dec. 2018.

[22] M. Zinkevich, "Thermodynamics of rare earth sesquioxides," *Prog. Mater. Sci.*, vol. 52, no. 4, pp. 597–647, May 2007.

[23] J. A. Palmer, K. Kreutz-Delgado, and S. Makeig, "AMICA: An adaptive mixture of independent component analyzers with shared components," Swartz Center Computatonal Neursoscience, Univ. California San Diego, San Diego, CA, USA, Tech. Rep., 2012.

[24] A. Delorme, J. Palmer, J. Onton, R. Oostenveld, and S. Makeig, "Independent EEG sources are dipolar," *PLoS ONE*, vol. 7, no. 2, Feb. 2012, Art. no. e30135.

[25] H. Leutheuser, F. Gabsteiger, F. Hebenstreit, P. Reis, M. Lochmann, and B. Eskofier, "Comparison of the AMICA and the InfoMax algorithm for the reduction of electromyogenic artifacts in EEG data," in *Proc. 35th Annu. Int. Conf. IEEE Eng. Med. Biol. Soc. (EMBC)*, Jul. 2013, pp. 6804–6807.

[26] B. B. Mandelbrot, *The Fractal Geometry of Nature*. San Francisco, CA, USA: W. H. Freeman, 1982.

[27] J. B. J. Fourier, *Théorie Analytique de la Chaleur*, 1822.

[28] M. T. Heideman, D. H. Johnson, and C. S. Burrus, "Gauss and the history of the fast Fourier transform," *Arch. Hist. Exact Sci.*, vol. 34, no. 3, pp. 265–277, 1985, doi: 10.1007/BF00348431.

[29] A. Haar, "Zur theorie der orthogonalen funktionensysteme," *Math. Ann.*, vol. 69, no. 3, pp. 331–371, Sep. 1910, doi: 10.1007/BF01456326.

[30] A. Grossmann and J. Morlet, "Decomposition of Hardy functions into square integrable wavelets of constant shape," *SIAM J. Math. Anal.*, vol. 15, no. 4, pp. 723–736, 1984, doi: 10.1137/0515056.

[31] A. Graps, "An introduction to wavelets," *IEEE Comput. Sci. Eng.*, vol. 2, no. 2, pp. 50–61, Jun. 1995.

[32] I. Daubechies, "The wavelet transform, time-frequency localization and signal analysis," *IEEE Trans. Inf. Theory*, vol. 36, no. 5, pp. 961–1005, Feb. 1990.

[33] I. Daubechies and J. C. Lagarias, "Two-scale difference equations. I. Existence and global regularity of solutions," *SIAM J. Math. Anal.*, vol. 22, no. 5, pp. 1388–1410, Sep. 1991, doi: 10.1137/0522089.

[34] I. Daubechies and J. C. Lagarias, "Two-scale difference equations II. Local regularity, infinite products of matrices and fractals," *SIAM J. Math. Anal.*, vol. 23, no. 4, pp. 1031–1079, Jul. 1992, doi: 10.1137/0523059.

[35] I. Daubechies, *Ten Lectures on Wavelets* (CBMS-NSF Regional Conference Series in Applied Mathematics). Philadelphia, PA, USA: SIAM, 1992. [Online]. Available: http://www.loc.gov/catdir/enhancements/fy0664/92013201-d.html

[36] R. Yan, R. X. Gao, and X. Chen, "Wavelets for fault diagnosis of rotary machines: A review with applications," *Signal Process.*, vol. 96, pp. 1–15, Mar. 2014. [Online]. Available: http://www.sciencedirect.com/science/article/pii/S0165168413001588

[37] J. Antonino-Daviu, P. Jover, M. Riera, A. Arkkio, and J. Roger-Folch, "DWT analysis of numerical and experimental data for the diagnosis of dynamic eccentricities in induction motors," *Mech. Syst. Signal Process.*, vol. 21, no. 6, pp. 2575–2589, Aug. 2007. [Online]. Available: http://www.sciencedirect.com/science/article/pii/S0888327007000301

[38] Z. R. Struzik and A. P. J. M. Siebes, "Wavelet transform based multifractal formalism in outlier detection and localisation for financial time series," *Phys. A, Stat. Mech. Appl.*, vol. 309, nos. 3–4, pp. 388–402, Jun. 2002. [Online]. Available: http://www.sciencedirect.com/science/article/pii/S0378437102005526

[39] M. Rabbani and R. Joshi, "An overview of the JPEG 2000 still image compression standard," *Signal Process., Image Commun.*, vol. 17, no. 1, pp. 3–48, Jan. 2002. [Online]. Available: http://www.sciencedirect.com/science/article/pii/S0923596501000248

[40] D. Taubman, E. Ordentlich, M. Weinberger, and G. Seroussi, "Embedded block coding in JPEG 2000," *Signal Process., Image Commun.*, vol. 17, no. 1, pp. 49–72, Jan. 2002. [Online]. Available: http://www.sciencedirect.com/science/article/pii/S0923596501000285

[41] P. Agrawal, M. Vatsa, and R. Singh, "Saliency based mass detection from screening mammograms," *Signal Process.*, vol. 99, pp. 29–47, Jun. 2014. [Online]. Available: http://www.sciencedirect.com/science/article/pii/S0165168413004982

[42] P. G. Nes, "Fast multi-scale edge-detection in medical ultrasound signals," *Signal Process.*, vol. 92, no. 10, pp. 2394–2408, Oct. 2012. [Online]. Available: http://www.sciencedirect.com/science/article/pii/S016516841200076X

[43] D. Cvetkovic, E. D. Übeyli, and I. Cosic, "Wavelet transform feature extraction from human PPG, ECG, and EEG signal responses to ELF PEMF exposures: A pilot study," *Digit. Signal Process.*, vol. 18, no. 5, pp. 861–874, Sep. 2008. [Online]. Available: http://www.sciencedirect.com/science/article/pii/S1051200407000978

[44] N. Hazarika, J. Z. Chen, A. C. Tsoi, and A. Sergejew, "Classification of EEG signals using the wavelet transform," *Signal Process.*, vol. 59, no. 1, pp. 61–72, May 1997. [Online]. Available: http://www.sciencedirect.com/science/article/pii/S0165168497000388

[45] D. Popivanov, S. Jivkova, V. Stomonyakov, and G. Nicolova, "Effect of independent component analysis on multifractality of EEG during visual-motor task," *Signal Process.*, vol. 85, no. 11, pp. 2112–2123, Nov. 2005. [Online]. Available: http://www.sciencedirect.com/science/article/pii/S0165168405002045

[46] C. Porcaro, M. Marino, S. Carozzo, M. Russo, M. Ursino, V. Ruggiero, C. Ragno, S. Proto, and P. Tonin, "Fractal dimension feature as a signature of severity in disorders of consciousness: An EEG study," *Int. J. Neural Syst.*, vol. 32, no. 7, Jul. 2022, Art. no. 2250031.

[47] S. V. Murav'eva, "Fractal structure of brain electrical activity of patients with mental disorders," *Frontiers Physiol.*, vol. 13, pp. 1–12, Jul. 2022, doi: 10.3389/fphys.2022.905318.

[48] C. S. Burrus, R. A. Gopinath, and H. Guo, *Introduction to Wavelets and Wavelet Transforms: A Primer*. Upper Saddle River, NJ, USA: Prentice-Hall, 1998.

[49] S. Jaffard, B. Lashermes, and P. Abry, "Wavelet leaders in multifractal analysis," in *Wavelet Analysis and Applications*. Basel, Switzerland: Birkhäuser, 2007, pp. 201–246, doi: 10.1007/978-3-7643-7778-6_17.

[50] B. Efron, "Bootstrap methods: Another look at the jackknife," *Ann. Statist.*, vol. 7, no. 1, pp. 1–26, Jan. 1979, doi: 10.1214/aos/1176344552.

[51] H. Wendt, P. Abry, and S. Jaffard, "Bootstrap for empirical multifractal analysis," *IEEE Signal Process. Mag.*, vol. 24, no. 4, pp. 38–48, Jul. 2007.

[52] R. F. Leonarduzzi, M. E. Torres, and P. Abry, "Scaling range automated selection for wavelet leader multifractal analysis," *Signal Process.*, vol. 105, pp. 243–257, Dec. 2014. [Online]. Available: http://www.sciencedirect.com/science/article/pii/S0165168414002680

[53] G. Lancaster, D. Iatsenko, A. Pidde, V. Ticcinelli, and A. Stefanovska, "Surrogate data for hypothesis testing of physical systems," *Phys. Rep.*, vol. 748, pp. 1–60, Jul. 2018. [Online]. Available: https://www.sciencedirect.com/science/article/pii/S0370157318301340

[54] J. W. Kantelhardt, E. Koscielny-Bunde, H. H. A. Rego, S. Havlin, and A. Bunde, "Detecting long-range correlations with detrended fluctuation analysis," *Phys. A, Stat. Mech. Appl.*, vol. 295, nos. 3–4, pp. 441–454, Jun. 2001. [Online]. Available: https://www.sciencedirect.com/science/article/pii/S0378437101001443

[55] J. W. Kantelhardt, S. A. Zschiegner, E. Koscielny-Bunde, S. Havlin, A. Bunde, and H. E. Stanley, "Multifractal detrended fluctuation analysis of nonstationary time series," *Phys. A, Stat. Mech. Appl.*, vol. 316, nos. 1–4, pp. 87–114, Dec. 2002. [Online]. Available: https://www.sciencedirect.com/science/article/pii/S0378437102013833

[56] E. A. F. Ihlen, "Introduction to multifractal detrended fluctuation analysis in MATLAB," *Frontiers Physiol.*, vol. 3, pp. 1–12, Mar. 2012, doi: 10.3389/fphys.2012.00141.

[57] N. Mammone, F. La Foresta, and F. C. Morabito, "Automatic artifact rejection from multichannel scalp EEG by wavelet ICA," *IEEE Sensors J.*, vol. 12, no. 3, pp. 533–542, Mar. 2012.

[58] N. P. Castellanos and V. A. Makarov, "Recovering EEG brain signals: Artifact suppression with wavelet enhanced independent component analysis," *J. Neurosci. Methods*, vol. 158, no. 2, pp. 300–312, Dec. 2006.

[59] M. H. Soomro, N. Badruddin, M. Z. Yusoff, and A. S. Malik, "A method for automatic removal of eye blink artifacts from EEG based on EMD-ICA," in *Proc. IEEE 9th Int. Colloq. Signal Process. Appl.*, Mar. 2013, pp. 129–134.

[60] P. Li, Z. Chen, and Y. Hu, "A method for automatic removal of EOG artifacts from EEG based on ICA-EMD," in *Proc. Chin. Autom. Congr. (CAC)*, Oct. 2017, pp. 1860–1863.

[61] S. K. Noorbasha and G. F. Sudha, "Removal of EOG artifacts and separation of different cerebral activity components from single channel EEG—An efficient approach combining SSA–ICA with wavelet thresholding for BCI applications," *Biomed. Signal Process. Control*, vol. 63, Jan. 2021, Art. no. 102168.

[62] A. Delorme and S. Makeig, "EEGLAB: An open source toolbox for analysis of single-trial EEG dynamics including independent component analysis," *J. Neurosci. Methods*, vol. 134, no. 1, pp. 9–21, Mar. 2004.

[63] I. Marriott Haresign, E. Phillips, M. Whitehorn, V. Noreika, E. J. H. Jones, V. Leong, and S. V. Wass, "Automatic classification of ICA components from infant EEG using MARA," *Develop. Cognit. Neurosci.*, vol. 52, Dec. 2021, Art. no. 101024.

[64] L. Pion-Tonachini, K. Kreutz-Delgado, and S. Makeig, "ICLabel: An automated electroencephalographic independent component classifier, dataset, and website," *NeuroImage*, vol. 198, pp. 181–197, Sep. 2019.

[65] G. Gómez-Herrero, "Automatic artifact removal (AAR) toolbox v1. 3 (release 09.12. 2007) for MATLAB," Tampere Univ. Technol., Tampere, Finland, Tech. Rep., 2007.

[66] M. A. Klados, C. Papadelis, C. Braun, and P. D. Bamidis, "REG-ICA: A hybrid methodology combining blind source separation and regression techniques for the rejection of ocular artifacts," *Biomed. Signal Process. Control*, vol. 6, no. 3, pp. 291–300, Jul. 2011.

[67] S. Leske and S. S. Dalal, "Reducing power line noise in EEG and MEG data via spectrum interpolation," *NeuroImage*, vol. 189, pp. 763–776, Apr. 2019.

[68] J. Urigüen and B. Garcia-Zapirain, "EEG artifact removal-state-of-the-art and guidelines," *J. Neural Eng.*, vol. 12, no. 3, 2015, Art. no. 031001.

[69] R. Mahajan and B. I. Morshed, "Sample entropy enhanced wavelet-ICA denoising technique for eye blink artifact removal from scalp EEG dataset," in *Proc. 6th Int. IEEE/EMBS Conf. Neural Eng. (NER)*, Nov. 2013, pp. 1394–1397.

BECHIR HBIBI received the master's degree in electronics, electro-technics, and automatics, with a focus on hyper-frequency antennas. He is currently pursuing the Ph.D. degree in electronics with the University of Tunis El Manar. He was involved/trained with the EEG Center, National Institute of Neurology, Tunis, and the Department of Electrical and Computer Engineering, Northern Virginia Center, Virginia Tech. He has online certifications in neurology and brain activity. His research interests include comatose human brain activity and classification.

CYRINE KHIARI received the master's degree in electronics, electro-technics, and automatics. She is currently pursuing the Ph.D. degree in electronics with the University of Tunis El Manar. She was involved/trained with the Department of Electrical and Computer Engineering, Northern Virginia Center, Virginia Tech. Her research interest includes the application of machine learning to electroencephalography signals.

KARLTON WIRSING (Senior Member, IEEE) received the degree in information assurance, the master's degree in computer science, the master's degree in electrical engineering, and the Ph.D. degree in electrical engineering from Virginia Polytechnic Institute and State University. He was involved in various industries doing software development for more than 20 years. He is currently a licensed Professional Engineer in Virginia. His research interests include multifractal analysis, chaotic phenomenon, wavelet analysis, machine learning, and high-performance computing. He is a Senior Member of AIAA and a member of ACM and SIAM. He has been selected to serve on the AIAA Software Technical Committee.

LAMINE MILI (Life Fellow, IEEE) is currently a Professor and the Program Director of the Department of Electrical and Computer Engineering, Northern Virginia Center, Virginia Tech. He was a Visiting Professor with the Swiss Federal Institute of Technology Lausanne, Switzerland; the Grenoble Institute of Technology; École supérieure d'électricité, France; and École Polytechnique de Tunisie, Tunisia, and did consulting work for Hydro-Québec and French Power Transmission Company, RTE. He has published more than 150 hundred technical articles and edited two books. His research interests include robust estimation and control, robust Kalman filtering, copula indices, risk management of complex systems to catastrophic failures, non-linear dynamics, and bifurcation theory.

KAMEL BACCAR has been a Major Specialist Physician with the Intensive Care and Anesthesia Department, National Institute of Neurology, since 2004. In addition, to his activities in neuro-reanimation, neuroradiological, and neurosurgical anesthesia. He has been a local referent Physician for the promotion of organ donation and transplantation with CNPTO, since 2007. He is currently a member of a university research brain unit. He has coauthored several abstracts, journal articles, and a book specializing in neuro-reanimation. He was an elected member of the medical committee for several terms and a member of the scientific committees of the institute, known as Therapeutics: Fight Against Nosocomial.

ABDELKADER MAMI received the Dissertation H.D.R. (Enabling to Direct Research) from the University of Lille, France, in 2003. He is currently a Professor and the Department Head of the Faculty of Sciences of Tunis, University of Tunis El Manar, Tunis, Tunisia. He is a Member of Scientific Advisor and the President of the thesis committee of electronics with the Faculty of Sciences of Tunis. He is also the Director of the Laboratory of the Energy Efficiency and Renewable Energies (LAPER), Tunis. His research interests include photovoltaic power systems, hybrid power systems, power generation control, renewable energy sources, and proton exchange membrane fuel cells.

• • •